




# Stromal Collagen Content in Breast Tumors Correlates With In Vivo Diffusion-Weighted Imaging: A Comparison of Multi *b*-Value DWI With Histologic Specimen From Benign and Malignant Breast Lesions

Liv Egnell, MSc,<sup>1,2</sup>  Igor Vidić, PhD,<sup>1</sup> Neil P. Jerome, PhD,<sup>2,3</sup>  Anna M. Bofin, MD, PhD,<sup>4</sup> Tone F. Bathen, PhD,<sup>2,3</sup>  and Pål Erik Goa, PhD<sup>1,2\*</sup>

**Background:** Increased deposition and reorientation of stromal collagen fibers are associated with breast cancer progression and invasiveness. Diffusion-weighted imaging (DWI) may be sensitive to the collagen fiber organization in the stroma and could provide important biomarkers for breast cancer characterization.

**Purpose:** To understand how collagen fibers influence water diffusion in vivo and evaluate the relationship between collagen content and the apparent diffusion coefficient (ADC) and the signal fractions of the biexponential model using a high *b*-value scheme.

**Study Type:** Prospective.

**Subjects/Specimens:** Forty-five patients with benign ( $n = 8$ ), malignant ( $n = 36$ ), and ductal carcinoma in situ ( $n = 1$ ) breast tumors. Lesions and normal fibroglandular tissue ( $n = 9$ ) were analyzed using sections of formalin-fixed, paraffin-embedded tissue stained with hematoxylin, erythrosine, and saffron.

**Field Strength/Sequence:** MRI (3T) protocols: *Protocol I:* Twice-refocused spin-echo echo-planar imaging with: echo time (TE) 85 msec; repetition time (TR) 9300/11600 msec; matrix  $90 \times 90 \times 60$ ; voxel size  $2 \times 2 \times 2.5 \text{ mm}^3$ ; *b*-values: 0 and  $700 \text{ s/mm}^2$ . *Protocol II:* Stejskal–Tanner spin-echo echo-planar imaging with: TE: 88 msec; TR: 10600/11800 msec, matrix  $90 \times 90 \times 60$ ; voxel size  $2 \times 2 \times 2.5 \text{ mm}^3$ ; *b*-values [0, 200, 600, 1200, 1800, 2400, 3000]  $\text{s/mm}^2$ .

**Assessment:** Area fractions of cellular and collagen content in histologic sections were quantified using whole-slide image analysis and compared with the corresponding DWI parameters.

**Statistical Tests:** Correlations were assessed using Pearson's *r*. Univariate analysis of group median values was done using the Mann–Whitney *U*-test.

**Results:** Collagen content correlated with the fast signal fraction ( $r = 0.67$ ,  $P < 0.001$ ) and ADC ( $r = 0.58$ ,  $P < 0.001$ ) and was lower ( $P < 0.05$ ) in malignant lesions than benign and normal tissues. Cellular content correlated inversely with the fast signal fraction ( $r = -0.67$ ,  $P < 0.001$ ) and ADC ( $r = -0.61$ ,  $P < 0.001$ ) and was different ( $P < 0.05$ ) between malignant, benign, and normal tissues.

**Data Conclusion:** Our findings suggest stromal collagen content increases diffusivity observed by MRI and is associated with higher ADC and fast signal fraction of the biexponential model.

**Level of Evidence:** 3

**Technical Efficacy Stage:** 3

J. MAGN. RESON. IMAGING 2019.

View this article online at [wileyonlinelibrary.com](http://wileyonlinelibrary.com). DOI: 10.1002/jmri.27018

Received Sep 13, 2019, Accepted for publication Nov 22, 2019.

\*Address reprint requests to: P.E.G., Department of Physics, Faculty of Natural Sciences, NTNU – Norwegian University of Science and Technology, Trondheim, Norway. E-mail: [pal.e.goa@ntnu.no](mailto:pal.e.goa@ntnu.no)

Contract grant sponsor: Liaison Committee between the Central Norway Regional Health Authority (RHA) and the Norwegian University of Science and Technology (NTNU).

From the <sup>1</sup>Department of Physics, NTNU – Norwegian University of Science and Technology, Trondheim, Norway; <sup>2</sup>Clinic of Radiology and Nuclear Medicine, St. Olav's University Hospital, Trondheim, Norway; <sup>3</sup>Department of Circulation and Medical Imaging, NTNU – Norwegian University of Science and Technology, Trondheim, Norway; and <sup>4</sup>Department of Clinical and Molecular Medicine, NTNU – Norwegian University of Science and Technology, Trondheim, Norway

This is an open access article under the terms of the Creative Commons Attribution-NonCommercial License, which permits use, distribution and reproduction in any medium, provided the original work is properly cited and is not used for commercial purposes.

**B**REAST CANCER is the most commonly diagnosed cancer among women worldwide, and a leading cause of cancer death.<sup>1</sup> The disease is clinically and biologically heterogeneous, which is reflected in the observed histopathology, molecular subtypes, therapeutic response, metastatic patterns, and ultimately in disease outcome. The specific treatment choice is based on tumor size and extent, measured by imaging modalities including magnetic resonance imaging (MRI), histopathological grade,<sup>2</sup> and tissue biomarkers including proliferation index (Ki67), estrogen and progesterone receptors (ER, PR) status, expression of human epidermal growth factor receptor 2 (HER2), and the presence of lymph node metastases.<sup>3,4</sup> Breast lesion characterization is essential for selecting the appropriate therapy and remains one of the major challenges in breast cancer treatment.

Breast cancer predominantly arises from epithelial cells in the ducts and lobules. The cancer cells interact closely with the tumor microenvironment, which consists of both a cellular, i.e. stromal cells, and a noncellular component, i.e. the extracellular matrix (ECM).<sup>5</sup> Today, the role of crosstalk between the epithelial and stromal components of breast cancer is acknowledged.<sup>6,7</sup>

Collagen is a major component of the ECM in normal fibroglandular tissue (FGT) in the breast, and changes in the structure and deposition of collagen are associated with breast cancer progression and invasiveness.<sup>8,9</sup> High collagen density in breast tissue is associated with mammographic breast density and an increased risk of developing invasive breast carcinoma.<sup>10</sup> In the normal mammary gland, the collagen fibers surrounding epithelial structures are typically curly and anisotropic, but in cancer the fibers progressively thicken and linearize at the tumor edge.<sup>8,9,11</sup> Remodeling of collagen is therefore an important pathological marker and a potential target for diagnostic imaging.

Diffusion-weighted imaging (DWI) MRI is a noninvasive imaging technique where endogenous contrast from water molecule motion is sensitized to tissue microstructural architecture. A simple, yet enduring, DWI-derived parameter is the apparent diffusion coefficient (ADC), requiring only a few acquisitions at low diffusion-weighting  $b$ -values ( $\leq 1000$  s/mm<sup>2</sup>); ADC is a valuable clinical diagnostic tool for discriminating malignant and benign lesions in the breast.<sup>12,13</sup> ADC is known to be inversely correlated with tissue cellularity in breast,<sup>12,14</sup> although ADC can be difficult to interpret since immune responses and changes in the extracellular environment also influence diffusion.

The ADC assumes Gaussian diffusion and models DWI signal as a monoexponential decay. In tissue, however, obstructions and restrictions imposed by tissue structures cause observable deviation from monoexponential decay, meaning that ADC fails to capture the full information available in DWI. In particular, this deviation becomes apparent with increasing diffusion weighting, with  $b$ -values beyond 1000 s/mm<sup>2</sup>.

Several mathematical expressions have been proposed to describe the observed attenuation of DWI signal at higher  $b$ -values. Diffusion kurtosis imaging studies suggest that high- $b$ -value measurements ( $b > 1000$  s/mm<sup>2</sup>) may provide additional value for breast lesion characterization.<sup>15</sup> Another DWI study in breast tumors found that modeling the signal using a biexponential model, comprising a weighted sum of two components with different apparent Gaussian diffusivities, correlated with cellular and extracellular contributions, with component magnitudes potentially influenced by the presence of hyalinized stromal collagen.<sup>16</sup> Although sharing the same functional form as the intravoxel incoherent motion (IVIM) model that reflects perfusion, the interpretation is reflective of different diffusion processes when applied to higher  $b$ -values (up to around 3000 s/mm<sup>2</sup>).

Current diffusion models do not include reference to collagen and the extracellular matrix, despite an expectation that these will influence diffusion properties. So far, only a few DWI studies have considered extracellular microstructural components in breast. A recent study in mice and ex vivo human breast cancer samples reported associations between collagen density and fractional anisotropy (FA) as well as ADC, both lowered in regions with sparse collagen fibers.<sup>17</sup> DWI may be sensitive to the collagen fiber organization in the stroma and chemotherapy outcome prediction.

The aim of this study was to investigate and determine the influence of collagen density in breast tumors on the signal observed in DWI at  $b$ -values up to 3000 s/mm<sup>2</sup> using the monoexponential and biexponential diffusion models.

## Materials and Methods

### Patient Cohort

This prospective study was approved by our institution (St. Olav's Hospital, Trondheim University Hospital) and the Regional Committee for Medical and Health Research Ethics, Central Norway (Identifier: 2011/568). All patients provided written informed consent before participation.

Forty-five patients were included in the analysis; details are provided in Table 1. Of the initial cohort of 90 patients, recruited and scanned between November 2012 and June 2016, 62 received surgery and provided lesion samples for histology. Some patients were excluded from analysis based on the following criteria: received neoadjuvant treatment ( $n = 3$ ), insufficient tumor material available for research ( $n = 3$ ), scarred tissue from previous plastic surgery ( $n = 1$ ), inability to define a suitable region of interest (ROI) in the histology slide ( $n = 2$ ), special histological type with mucinous component or mucinous-like appearance (mucinous carcinoma/phyllodes tumor:  $n = 1$  /  $n = 5$ ), and missing MRI data ( $n = 2$ ). Normal FGT was sampled in a subset of nine patients, where normal FGT was present both in the tissue sections and in the MRI images.

Final diagnosis, proliferation status (Ki67), and lymph node status were collected from the clinical excision biopsy report. ER, PR, and HER2 status were collected from the clinical needle biopsy report.

**TABLE 1. Descriptive Characteristics for the Patient Groups With Benign, Malignant, and Ductal Carcinoma In Situ Lesions and Normal Fibroglandular Tissue**

	Protocol I	Protocol II
<b>Malignant, <i>n</i></b>	36	17
Age median (IQR), years	54.5 (48–63)	52 (44–61.25)
Age (years), <i>n</i>		
<50	13	7
50–59	8	3
60–69	12	7
70–79	3	0
Time between MRI and surgery, days		
Median (IQR)	8 (6–13)	9 (4.25–12)
Range	1–35	1–35
Type, <i>n</i>		
No special type	33	15
Medullary carcinoma	2	1
Tubular carcinoma	1	1
Lymph node status, <i>n</i>		
Positive	15	4
Negative	21	13
Grade, <i>n</i>		
1	5	3
2	16	7
3	15	7
Ki67, <i>n</i>		
Positive	29	12
Negative	7	5
ER, <i>n</i>		
Positive	34	16
Negative	2	1
PR, <i>n</i>		
Positive	25	12
Negative	11	5

**TABLE 1. Continued**

	Protocol I	Protocol II
HER2, <i>n</i>		
Positive	9	5
Negative	27	12
<b>Ductal carcinoma in situ, <i>n</i></b>	1	1
Age, years	30	30
Time between MRI and surgery, days	22	22
<b>Benign, <i>n</i></b>	8	2
Age, median (IQR), years	24.5 (23–44)	24.5 (24–25)
Time between MRI and surgery, days		
Median (IQR)	92 (13.5–124.5)	51 (15–87)
Range	12–195	15–87
Type, <i>n</i>		
Fibroadenoma	7	1
Benign		
myoepithelioma	1	1
<b>Normal fibroglandular tissue, <i>n</i></b>	9	5
Age median (IQR), years	52 (49–61.25)	61 (58.0–62.5)

Immunohistochemical staining for proliferation status (Ki67) was considered positive if  $\geq 15\%$  of the nuclei were positively stained.<sup>39,40</sup> HER2 status was assessed by either fluorescence in situ hybridization (FISH) or immunohistochemistry (IHC; HercepTest) and was considered positive if the gene to chromosome ratio was  $\geq 2.0$  (FISH) or the IHC score was 3+. The cohort did not include any borderline cases with IHC score 2+. IQR, interquartile range; ER, estrogen receptor status; PR, progesterone receptor status; HER2, human epidermal growth factor receptor 2 status.

Previous published studies using patients from the initial cohort focused on diffusion modeling at low *b*-values and distortion correction techniques, using neither the higher *b*-value data nor histological data analyzed in this study.<sup>13,18–21</sup>

### MRI and Postprocessing

Imaging was performed with a 3T clinical MR scanner equipped with a 16-channel breast coil (Siemens Skyra, Erlangen, Germany).

As part of a more extensive research protocol, also including  $T_2$ -weighted and dynamic contrast-enhanced (DCE) imaging sequences, the examination included two DWI protocols:

**Protocol I:** Unilateral sagittal DWI was performed using a twice-refocused spin-echo sequence with echo-planar imaging read-out and included the following parameters: fat-suppression using FatSat/SPAIR: ( $n = 37 / n = 8$ ); repetition time (TR) = 9300/11600 msec; echo time (TE) = 85 msec; matrix  $90 \times 90 \times 60$ ; voxel size  $2 \times 2 \times 2.5$  mm; generalized autocalibrating partially parallel acquisition (GRAPPA) factor 2; anteroposterior phase-encoding; diffusion-encoding with 30 directions;  $b$ -values: 0 and  $700 \text{ s/mm}^2$ ; and one additional acquisition at  $b = 0 \text{ s/mm}^2$  with reversed phase-encoding direction. The total scan time was 10 min 32 sec / 13 min 9 sec.

**Protocol II:** Unilateral sagittal DWI was acquired using a Stejskal–Tanner spin-echo echo-planar imaging sequence with parameters: fat-suppression using FatSat/SPAIR: ( $n = 13 / n = 7$ ); TR = 10600/11800 msec ( $n = 14 / n = 8$ ); TE = 88 msec; matrix  $90 \times 90 \times 60$ ; voxel size  $2 \times 2 \times 2.5$  mm; GRAPPA factor 2; diffusion-encoding: six directions;  $b$ -values: [0, 200, 600, 1200, 1800, 2400, 3000]  $\text{s/mm}^2$  plus one additional acquisition at  $b = 0 \text{ s/mm}^2$  with reversed phase-encoding direction. Scan time was 7 min 46 sec / 8 min 39 sec. Protocol II was added to the scanning protocol in August 2014 and used for patients recruited subsequently.

### Image Processing and Analysis

Protocol I images with substantial motion artifacts were corrected using a normalized cross-correlation metric<sup>22</sup> and corrected for geometric distortions using the  $b = 0$  image with reversed phase encoding as described previously.<sup>19,23</sup> Protocol II images were corrected for geometric distortion,<sup>23</sup> eddy current artifacts, and motion using in-house software developed at the University of California San Diego.<sup>24</sup> Subsequently, noise floor correction for Protocol II was performed in order to address the low signal observed at the highest  $b$ -values. A corrected and normalized signal intensity,  $SI_{\text{corr}}$ , was calculated in each individual voxel for each measured  $b$ -value and diffusion-encoding direction by:

$$SI_{\text{corr}} = \begin{cases} \frac{1}{SI_{\text{bkg}}} \sqrt{SI_{\text{obs}}^2 - SI_{\text{bkg}}^2}, & SI_{\text{obs}} > SI_{\text{bkg}} \\ 0, & SI_{\text{obs}} \leq SI_{\text{bkg}} \end{cases} \quad (1)$$

where  $SI_{\text{obs}}$  is the observed signal and  $SI_{\text{bkg}}$  is the background intensity defined as the mean intensity inside an ROI covering the whole breast at  $b = 3000 \text{ s/mm}^2$  in each patient. This approach is equivalent to the method described by Karunamuni et al,<sup>25</sup> but modified to use the healthy tissue signal at  $b = 3000 \text{ s/mm}^2$  (which can be assumed to be zero given the known ADC) instead of signal measured in air. The normalization factor  $1/SI_{\text{bkg}}$  was introduced in order to avoid the effect of different image intensity scaling between the FatSat and SPAIR protocols.

ROIs for the lesions were manually delineated in the  $b = 700 \text{ s/mm}^2$  (Protocol I) and  $b = 600 \text{ s/mm}^2$  (Protocol II) images in all slices, producing a 3D volume of interest (VOI) for each lesion. The corresponding DCE images were used as a visual guide. Where multiple lesions were present in the same breast, the largest was selected for analysis. Lesion delineation was performed by scientists with 3 or

more years' experience in breast cancer MRI, with supervision by an experienced breast radiologist.

Voxelwise ADC was obtained with a standard DWI fitting using  $S_{b700} = S_{b0} \exp(-b \cdot \text{ADC})$  with signal values from the trace-weighted DWI images at  $b = 0$  and  $b = 700 \text{ s/mm}^2$  from Protocol I, as described in a previous study.<sup>18</sup> The mean value for each VOI was used for the statistical analysis.

The biexponential model describes the signal as the superposition of two signal components:

$$S/S_{b0} = f_{\text{fast}} \exp(-b \cdot D_{\text{fast}}) + f_{\text{slow}} \exp(-b \cdot D_{\text{slow}}) \quad (2)$$

where  $D_{\text{fast}}$  and  $D_{\text{slow}}$  represent the fast and the slow apparent diffusion coefficients, which are commonly interpreted as reflective of extracellular and intracellular water components, respectively. The signal fractions  $f_{\text{fast}}$  and  $f_{\text{slow}}$  represent the weights of these components in the observed signal and are constrained by:

$$f_{\text{fast}} + f_{\text{slow}} = 1. \quad (3)$$

The parameters in the biexponential model were estimated from the Protocol II data using the corrected mean VOI signal intensity, for all diffusion-encoding directions, over the full range of measured  $b$ -values up to  $3000 \text{ s/mm}^2$ , except  $b = 0 \text{ s/mm}^2$ , which was excluded to avoid influence from perfusion. The parameters were derived in MatLab (MathWorks, Natick, MA) by nonlinear least-squares fitting, with constraints applied to ensure correct separation between the two ADCs:  $D_{\text{slow}} \leq 0.5 \times 10^{-3} \text{ mm}^2/\text{s}$  and  $0.5 < D_{\text{fast}} < 5.0 \times 10^{-3} \text{ mm}^2/\text{s}$ . The division at  $0.5 \times 10^{-3} \text{ mm}^2/\text{s}$  was chosen because this is below the lowest ADC values typically observed in breast lesions using a monoexponential model. The upper limit was set to  $5 \times 10^{-3} \text{ mm}^2/\text{s}$  in order to avoid nonphysical values.

### Proton Density Estimates

The short  $T_2$  relaxation times observed in collagen-rich tissues, such as cartilage (20–40 msec<sup>26</sup>), causes poor signal-to-noise ratio (SNR) in spin-echo DWI in vivo measurements due to the long echo times required. To verify that we received signal from the collagenous stroma in the breast, we used conventional  $T_2$ -weighted images to estimate the relative proton density of normal FGT. First, the mean MRI signal intensities at  $b = 0 \text{ s/mm}^2$  and TE = 85 msec (Protocol I) from ROIs from patients with normal FGT ( $n = 7$ ) and cysts ( $n = 3$ ) were measured. The nominal signal intensities at TE = 0 msec could then be estimated using the relation  $S(\text{TE}) = S_{\text{TE=0}} \exp(-\text{TE}/T_2)$  and inserting averaged  $T_2$ -values, obtained from the literature, of 63 msec measured in normal FGT<sup>27,28</sup> and 617 msec for cysts measured in brain.<sup>29</sup> By taking the proton density of cysts, which appear bright in the  $T_2$ -weighted images and have a high proton density, the relative water proton density in normal FGT can be estimated by the ratio between the two calculated signal intensities at TE = 0 msec.

### Histology and Whole-Slide Image Analysis

Formalin-fixed, paraffin-embedded tissue blocks from the tumors were collected from the clinical biobank. In the case of multiple lesions in the same breast, blocks from the largest lesion were selected for analysis and processed according to a standard protocol at our cellular and molecular imaging core facility. Sections of 4  $\mu\text{m}$

thickness were mounted on glass slides and stained with hematoxylin, erythrosine, and saffron (HES). As in H&E, hematoxylin stains cell nuclei in blue/purple and erythrosine stains cell cytoplasm and connective tissue fibers in shades of reddish-pink and erythrocytes red. The additional saffron stain gives the collagen fibers a yellow color. Whole-slide images of the HES-stained slides, with a pixel size of  $0.3447 \mu\text{m} \times 0.3447 \mu\text{m}$ , were acquired using a slide scanner (Olympus VSI120, Shinjuku, Tokyo, Japan) with a  $\times 20$  magnification objective lens.

The tumor ROIs were manually delineated to cover as much tumor as possible in each whole-slide image. In addition, ROIs of normal FGT were delineated from a subgroup of patients with ROIs at least 2 mm away from malignant lesions. All ROI delineations in the histological specimens were supervised and confirmed by an experienced pathologist (A.M.B., with more than 30 years of experience). The ROIs were delineated using QuPath,<sup>30</sup> and exported to MatLab for further analysis.

The first step in the segmentation process was to sample the three stain colors and the white background in the histology slide. ROIs providing a reference color for each class were manually delineated in one representative whole-slide image and their mean RGB values were used as input to the segmentation algorithm. Both the HES-images and the sampled input colors were then transformed to the International Commission on Illumination (CIE)  $L^*a^*b^*$  color-space, in which the  $a^*$  and  $b^*$  values define the color and  $L^*$  defines the luminance, or lightness. Maps of Euclidean distances in the  $a^*-b^*$  plane from each pixel color to each of the stain colors was calculated, and the pixels were assigned to the class associated with the smallest Euclidean distance. Discarding the  $L^*$  channel will mitigate the effect of systematic differences in overall lightness between the digital slides. Pixels belonging to regions that did not contain tissue (ie, white background regions), were excluded by a histogram-guided threshold in the RGB green channel.

The segmentation was performed on all pixels within the tumor and normal FGT ROIs, where each pixel was classified into one of the five classes: 1) cellular content stained by hematoxylin; 2) erythrocytes, stained by erythrosine; 3) collagen content stained by saffron; 4) other tissue components; and 5) background, representing spaces with no tissue present. The background class does not have a unique interpretation in an in vivo context. Several artifacts introduced by the sample preparation leaves empty white spaces in the slide, including: ruptures from sectioning, tissue shrinkage, and the removal of soluble substances by solvents, as, for example, the lipid content of fat cells that are dissolved by ethanol. For this reason, the background class was excluded from further analysis.

Area fractions for the remaining four tissue classes were calculated by summing up all pixels belonging to the given class and dividing them by the sum of all pixels representing tissue:

$$AF_c = \frac{N_c}{N_1 + N_2 + N_3 + N_4} \quad (4)$$

where  $AF_c$  is the area fraction of class  $c$  and  $N_c$  is the number of pixels in class  $c$ . The whole-slide image segmentation was performed using an in-house developed program in MatLab.

## Statistical Tests

The Pearson correlation coefficient ( $r$ ) was used to test for a correlation between the area fractions of the different tissue stains and parameters derived from DWI. The Mann–Whitney  $U$ -test was used for univariate analysis of group median values.  $P < 0.05$  was considered significant.

## Results

The final study cohort consisted of 45 patients (8 benign, 36 malignant, and 1 ductal carcinoma in situ [DCIS]). High  $b$ -value DWI measurements (Protocol II) were acquired for a subset of 20 patients (2 benign, 17 malignant, and 1 DCIS). A detailed description of the patient cohort is given in Table 1. DCIS was categorized in a separate group as it is a noninvasive breast carcinoma that remains in the milk ducts and is not defined as a cancer by the World Health Organization. The data from the single case of DCIS was included in the correlation analysis but was not considered in the comparisons of group medians. Example images from the MRI acquisition of two patients, with invasive carcinoma of no special type and fibroadenoma, are shown in Fig. 1.

An example of a whole-slide histological image and ROI delineation is shown in Fig. 2, together with a higher-resolution detail shown alongside a visualization map of the segmentation of the corresponding region. Visual inspection of the classification was found to be excellent and successfully identified stained cells, collagen, and erythrocytes as well as other tissue components and background.

The measurements of histology area fractions arising from the segmentation analysis (Fig. 3) revealed two significant results. First, the median cellular area fraction was smaller in normal FGT (0.081) than in benign lesions (0.146) and largest in malignant lesions (0.329), with all comparisons being statistically significant. Second, the median collagen area fraction was larger in normal FGT (0.536) than in benign lesions (0.417), and smallest in malignant lesions (0.225). Differences were significant when comparing malignant with either benign or normal FGT.

The estimated area fractions of the third stain class, erythrosine, were very small (median area fraction, malignant: 0.0013, benign: 0.0022, normal: 0.0006), and were therefore not considered for comparison with ADC or the signal fractions of the biexponential model. Repeating the segmentation with class reference colors defined in different slices introduced some variations in absolute area fraction values, but gave consistent relative results.

Quantifications of ADC and the parameters of the biexponential model are summarized in Table 2. Both ADC and the fast signal fraction were found to be significantly smaller in malignant lesions than in benign lesions and normal FGT (Fig. 4). The low number of benign lesions in the Protocol II group is limiting ( $n = 2$ ), but it is notable that values for  $D_{\text{slow}}$  and  $f_{\text{fast}}$  were at the upper constraints. This

was not observed for either malignant lesions or normal FGT, indicating that convergence was achieved with the biexponential fitting for these two tissue types.

The scatterplot in Fig. 5a shows a moderate positive correlation between  $f_{\text{fast}}$  and collagen area fraction ( $r = 0.67$ ,  $P = 0.0003$ ). An inverse correlation of similar strength is observed between  $f_{\text{fast}}$  and cellular area fraction ( $r = -0.67$ ,  $P = 0.0003$ ) in Fig. 5b. The similarity in correlation strength between the two is remarkable but cannot be explained by the fact that the measured erythrosine area fraction is small, since the area fraction of tissue that did not take up stain cannot be neglected.

The corresponding scatterplots of ADC with the collagen and cellular area fractions (Fig. 5c,d) show similar trends to that observed for  $f_{\text{fast}}$ , although these are weaker, with moderate positive correlation coefficients between ADC and collagen ( $r = 0.58$ ,  $P < 0.0001$ ) and ADC and cellular area fraction ( $r = -0.61$ ,  $P < 0.0001$ ).

### Proton Density Estimates

From the measured signal intensities at  $b = 0 \text{ s/mm}^2$  and  $TE = 85 \text{ msec}$  in normal FGT and cysts, and resulting estimated signal intensities at  $TE = 0 \text{ msec}$ , shown in Table 3, we estimate the water proton density of the normal FGT to be approximately 86% of that in a cyst. This estimation may include influence from other factors, including coil sensitivity, but reliably illustrates the contribution to the overall water signal from FGT.

### Discussion

The exploration of the relationship between DWI parameters and tissue microstructure is important to improve our understanding of the DWI signal as a tool to characterize lesions. This study demonstrates and illuminates the association between cellular and stromal collagen content in breast tissue and DWI parameters, specifically ADC and the signal fractions of the biexponential model.

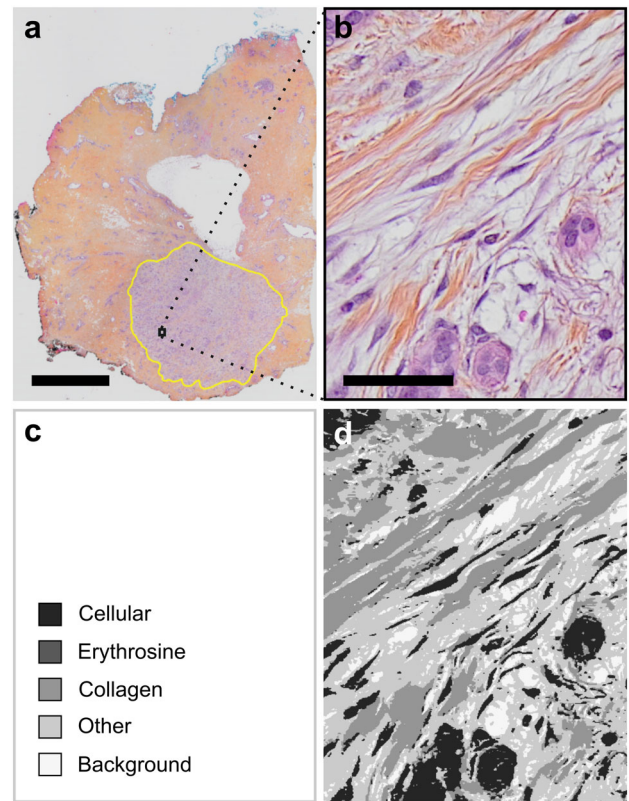


FIGURE 2: (a) Example of a whole-slide image with ROI delineation of an invasive carcinoma of no special type. Scale bar = 5 mm. (b) Region from the same slide at higher resolution. Original magnification  $\times 20$ . Scale bar = 50  $\mu\text{m}$ . (c) Legend showing the five grayscale values used for visualization of the segmentation. (d) Map showing the segmentation results of the region shown in (b).

Numerous studies have observed an inverse correlation between ADC and cellularity, i.e. nuclear count. The lower ADC in tumors with high cellularity is often thought to reflect hindrance and restrictions introduced by increased cellularity, with more densely packed cells. Our study confirms this link but uses relative cell area instead of cellularity to measure the cellular content. However, reported correlations between ADC

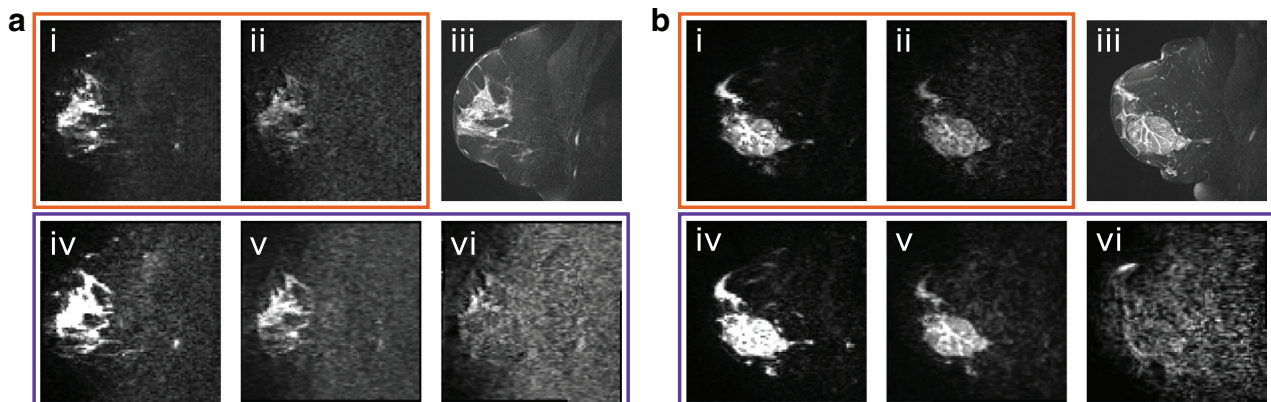
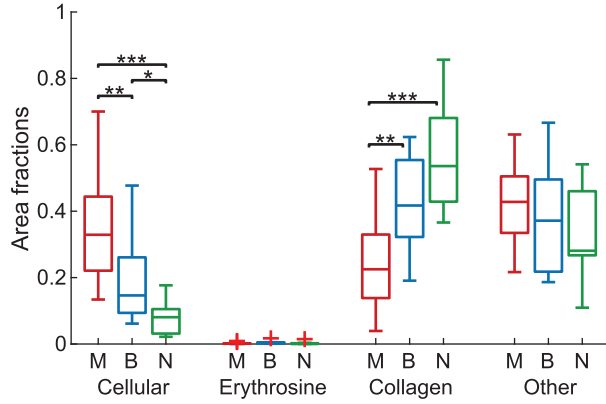


FIGURE 1: Examples of MRI images of (a) a patient with invasive carcinoma of no special type and (b) a patient with fibroadenoma. Latin numbers indicate the sequence used for acquisition: (i) Protocol I,  $b = 0 \text{ s/mm}^2$ . (ii) Protocol I,  $b = 700 \text{ s/mm}^2$ . (iii)  $T_2$ -weighted. (iv) Protocol II,  $b = 0 \text{ s/mm}^2$ . (v) Protocol II,  $b = 600 \text{ s/mm}^2$ . (vi) Protocol II,  $b = 1800 \text{ s/mm}^2$ .



**FIGURE 3: Area fractions of the four tissue classes obtained from segmentation of digital histology slides in malignant lesions (M;  $n = 36$ ), benign lesions (B;  $n = 8$ ), and normal fibroglandular tissue (N;  $n = 9$ ). The single case of DCIS was not included in this analysis. \* $P < 0.05$ , \*\* $P < 0.01$ , \*\*\* $P < 0.001$ .**

and cellular density varies between different organs.<sup>31</sup> In breast, reported correlations have typically been weak to moderate, and some even negligible.<sup>12,14,31</sup> This suggests that the lower ADC commonly observed in breast cancer lesions may not be explained solely by increased cellularity.

### Sensitivity of DWI to Stromal Changes

The results from this study add to the still relatively small body of literature that focus on extracellular microstructural

components in breast and which reflect the increasing interest in how DWI can be used to investigate stromal changes. We observed a significant positive correlation between ADC and stromal collagen content. This finding is consistent with that of Kakkad et al, who observed that ADC increased with higher collagen content.<sup>17</sup> We found that ADC was higher in normal FGT, which has a higher collagen content, than in malignant lesions, which have a lower collagen content. These results suggest that the decrease in water diffusivity may be related to the decrease in collagen content. One possible explanation for this relation could be increased diffusion along the direction of the collagen fibers, which has been observed with diffusion tensor imaging measurements.<sup>17</sup>

Similar to ADC, the fast signal fraction of the biexponential model correlated inversely with cellular content, and positively with collagen content. The correlation coefficients between the slow signal fraction and the histological area fractions are equal in magnitude to the correlation coefficients of the fast signal fraction but have inverse direction. The associated interpretation of this complementary relation is that the slow signal fraction comes from intracellular water, which is restricted by the cell membranes, and the fast signal fraction represents protons diffusing in the extracellular space.

Tamura et al<sup>32</sup> showed that the signal decay of malignant breast lesions could be well fitted with the biexponential model, while normal mammary glands, cysts, and some

**TABLE 2. Median and Interquartile Range (IQR) of ADC and the Parameters of the Biexponential Model Observed in Malignant and Benign Lesions and Normal Fibroglandular Tissue (FGT)**

MRI parameters, median (IQR)			
	Malignant	Benign	Normal FGT
ADC, $\times 10^{-3} \text{mm}^2/\text{s}$	1.04 (0.96–1.20)	1.75 (1.51–1.86)	1.71 (1.57–1.83)
$f_{\text{fast}}$	0.54 (0.52–0.62)	0.96 (0.92–1.00)	0.86 (0.82–0.89)
$D_{\text{fast}}$ , $\times 10^{-3} \text{mm}^2/\text{s}$	1.89 (1.60–2.10)	2.09 (1.84–2.34)	2.37 (2.19–2.52)
$D_{\text{slow}}$ , $\times 10^{-3} \text{mm}^2/\text{s}$	0.34 (0.25–0.48)	0.49 (0.49–0.49)	0.21 (0.06–0.22)

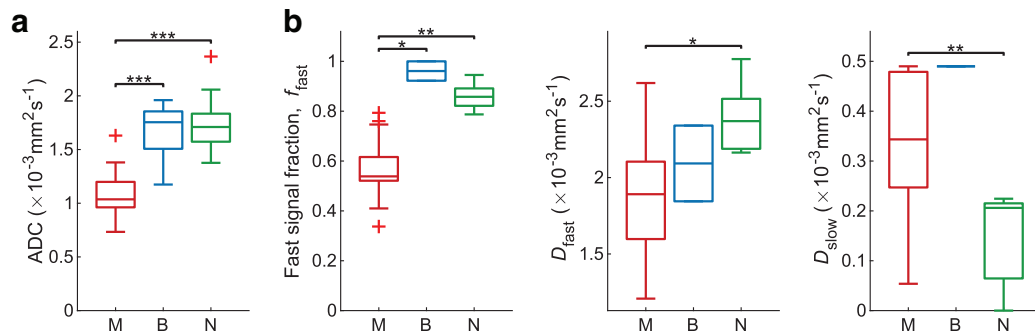


**FIGURE 4: (a) ADC in malignant (M;  $n = 36$ ) and benign (B;  $n = 8$ ) lesions and normal fibroglandular tissue (N;  $n = 9$ ). (b) DWI parameters  $f_{\text{fast}}$ ,  $D_{\text{fast}}$ , and  $D_{\text{slow}}$  from the biexponential model in malignant (M;  $n = 17$ ) and benign (B;  $n = 2$ ) lesions and normal fibroglandular tissue (N;  $n = 5$ ). The single case of DCIS was not included in this analysis. \* $P < 0.05$ , \*\* $P < 0.01$ , \*\*\* $P < 0.001$ .**

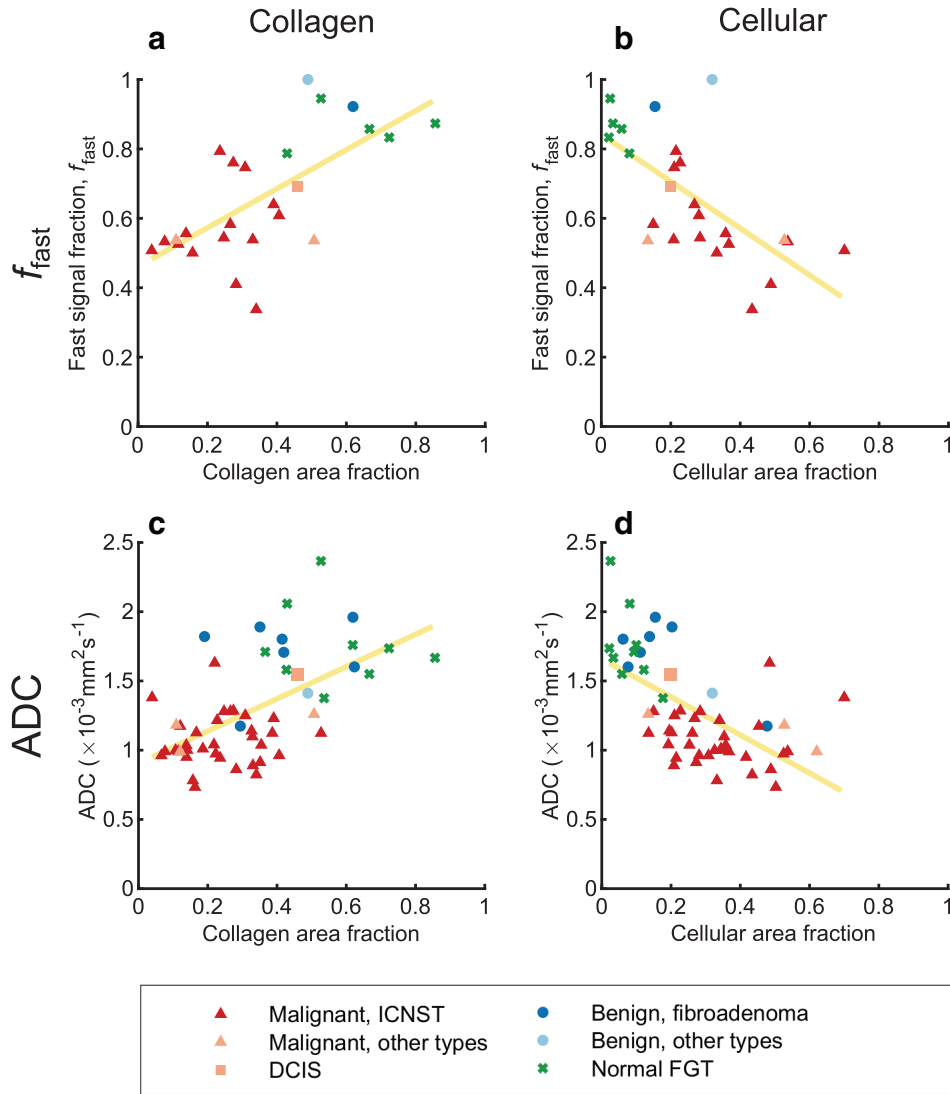


FIGURE 5: Scatterplots of DWI parameters and area fractions obtained from segmentation of the digital histology images. Marker shape and colors indicate tissue type. (a) Fast signal fraction against collagen area fraction ( $r = 0.67$ ,  $P = 0.0003$ ,  $n = 25$ ). (b) Fast signal fraction against cell area fraction ( $r = -0.67$ ,  $P = 0.0003$ ,  $n = 25$ ). (c) ADC against collagen area fraction ( $r = 0.58$ ,  $P < 0.0001$ ,  $n = 54$ ). (d) ADC against cellular area fraction ( $r = -0.61$ ,  $P < 0.0001$ ,  $n = 54$ ). ICNST, invasive carcinoma of no special type; DCIS, ductal carcinoma in situ; FGT, fibroglandular tissue.

TABLE 3. Mean Signal Intensity at  $b = 0 \text{ s/mm}^2$  in Normal Fibroglandular Tissue ( $n = 9$ ) and Cysts ( $n = 3$ )

	Signal intensity mean ( $\pm$ SD), a.u.	
	Normal FGT	Cysts
TE = 85 msec	84 ( $\pm$ 11)	328 ( $\pm$ 117)
TE = 0 msec*	324	376

The estimated signal intensity at TE = 0 msec indicates high water proton density also in the normal fibroglandular tissue.

\*Estimated from average of literature values for  $T_2$ : Normal FGT: 63 msec, Cyst: 617 msec. FGT, fibroglandular tissue; SD, standard deviation.

fibroadenomas followed a monoexponential attenuation. In our observations, we found that the biexponential model was able to describe the signal attenuation well for all lesions, although for some lesions the estimated parameters hit extreme values. For a few cases in the malignant and normal group, the observed ADC of the slow fraction reached the lower extreme limit, i.e.  $D_{\text{slow}} = 0 \times 10^{-3} \text{ mm}^2/\text{s}$ , yielding an essentially monoexponential fitted curve, which may indicate that the biexponential model is not appropriate to describe these cases. In the two benign lesions, the observed fast signal fraction was equal or close to the extreme upper limit, i.e.  $f_{\text{fast}} \approx 1$ , which indicates that their signal attenuation could also be well described by a monoexponential since the signal contribution from the slow diffusion component is very small. In



addition, their corresponding  $D_{\text{slow}}$  hit the upper constraint, which further supports that a simpler model could be more suitable for benign lesions. Therefore, it may be reasonable to exclude the benign lesions from the correlation analysis, which changes the correlation coefficient with  $f_{\text{fast}}$  to  $r = -0.76$  ( $P < 0.0001$ ) for cellular content, and  $r = 0.65$  ( $P = 0.0008$ ) for collagen content.

In another study,<sup>16</sup> the fast and slow signal components of the biexponential model were compared with the intra- and extracellular components obtained from histological H&E-stained specimens of breast cancers. Similar to our results, the authors found the slow signal component to be negatively correlated with the cellular fraction and positively correlated with the extracellular area fraction and the fast signal fraction. Interestingly, in their analysis of the histology they excluded any stromal regions containing collagen, based on the argument that tissues with high collagen content have short  $T_2$  and do not contribute significantly to the DWI signal.

While it is true that tissues with very aligned and densely packed collagen fibers, such as tendons, have a short  $T_2$  relaxation (0.25–22 msec), which varies with the orientation in relation to the applied magnetic field,<sup>33</sup>  $T_2$  in normal breast FGT is longer (50–70 msec).<sup>27,28</sup> The low signal intensity in  $T_2$ -weighted images in tendons can be explained by the highly organized collagen that binds and immobilizes water protons in combination with a fast proton-exchange between collagen-bound water molecules with freely diffusing water molecules in the surrounding environment.<sup>34</sup> In contrast to tendons, in which collagen can make up close to 100% of the total dry mass,<sup>35</sup> the collagen in breast is much less densely packed, and it is likely that only a fraction of bulk water molecules will interact with the collagen within the relevant time scale of the imaging.

To investigate this further, we estimated the water proton density in normal breast tissue, using the water proton density in breast cysts as a reference. We estimated the proton density in normal FGT to be approximately 86% of that of cysts, which have high water proton density. We found that the median collagen content in normal FGT was 54%, which indicates that at least part of the signal originates from tissue components where collagen is present. The self-diffusion coefficient of water diffusing freely is around  $3 \times 10^{-3}$  mm<sup>2</sup>/s at body temperature. A network of loosely organized collagen fibrils introduces hindrance (or increased tortuosity) and the diffusion coefficient should be slightly reduced. This is consistent with our observation of  $D_{\text{fast}}$  of around  $2 \times 10^{-3}$  mm<sup>2</sup>/s.

### Quantification of Collagen Content

Collagen content was quantitatively measured using automated segmentation on ROIs of benign and malignant lesions, and normal FGT in the digitized HES-stained histology slides. The image segmentation method used was similar

to the color classification method described previously,<sup>36</sup> which was shown to have high repeatability. The use of  $L^*a^*b^*$  space in the analysis separates lightness from the color values, which will reduce the variability in digital slides. Similar studies comparing diffusion MRI with histology typically use only a few fields of view rather than whole-slide images and are most commonly performed on slides stained only with H&E. Due to the heterogeneity in breast cancers, selecting fields of view in the histology that are representative for the lesion is inherently difficult and may be subjective. By using a whole-slide image approach, the risk of selection bias is reduced. In the more commonly used H&E-stained slides, collagen fibers are not specifically stained and therefore have a less distinct appearance. Hence, this information is less reliably available, which may be the reason why collagen has not been given much attention in the DWI literature, despite it being one of the major components in breast tissue and important for consideration of microstructure.

Collagen is closely associated with clinical outcome. A recent review summarized the role of collagen as a prognostic factor correlated with cancer differentiation, cancer invasion, lymph node metastasis, and clinical stage in cancer patients, including breast cancer.<sup>37</sup> Extensive collagen deposition, a main pathological characteristic of many cancers, could indicate that treatment with stromal targeting agents would be beneficial.<sup>38</sup> Thus, noninvasive characterization and biomarkers derived from a high  $b$ -value DWI scheme, capturing information on the collagen fibers, could have a role in treatment stratification and prediction of therapy response.

### Limitations

This study has several limitations. One important limitation is the small number of samples, especially for benign lesions. For nonsuspicious benign lesions, surgery is often not necessary, and if they are excised, they are usually larger in size. Another limitation is the time between MRI and surgery, with a median of 8 days for malignant cases, while for benign cases the median was 92 days (51 days for the subcohort also imaged with Protocol II). The longer waiting times for surgery of benign lesions is explained by the lack of urgency, as they are not invasive. We cannot exclude that biological or microstructural changes may occur within this time frame.

This study would have greatly benefited from a spatially matched voxelwise analysis, which would better account for heterogeneity across the tumor. A protocol for preserving lesion orientation information of the excised samples was included in the planning of the project to allow for colocalized measurements. Unfortunately, this information was found to be missing for most of the specimens for which standard clinical routines had been followed instead, and so this remains a natural progression of this work.

The application of larger diffusion-weightings, and for DWI studies in general, leads to a natural limit of available signal and thus the achievable resolution, meaning this approach will be challenging to apply for smaller lesions that are of clinical interest. Nevertheless, the findings of this research provide insights for the development of a specialized DWI protocol optimized for high  $b$ -value acquisitions in breast lesions.

## Conclusion

In conclusion, DWI has great potential to offer a noninvasive method to probe tissue microstructure at the cellular level. The microstructure and tissue composition of breast lesions and normal fibroglandular tissue is complex; in the ongoing search for adequate biophysical models to describe in vivo DWI, the optimal biophysical parameters have yet to be identified. The main aim of this study was to investigate the effects of how collagen contributes to the observed DWI signal in breast. The findings from this study make several contributions to the literature. First, our analysis includes multishell DWI data with  $b$ -values up to  $3000 \text{ s/mm}^2$ , which can be used to give DWI parameters that are more sensitive to collagen content than standard ADC measurements. Second, a whole-slide image approach was used to quantify the cellular and collagen content across the lesion, in order to avoid subjective or biased estimations. Third, explicit staining was used to directly quantify collagen content from the histology. The relevance of collagen for in vivo DWI is clearly supported by the current findings. Diffusion of water in collagen-rich regions was found to contribute to the measured DWI signal and affect the signal attenuation, which was reflected in both ADC and the fraction of the fast signal component of the biexponential model as measured in vivo. These findings suggest that diffusion MRI is sensitive to the collagen fiber organization in the stroma and support further validation of DWI as a noninvasive biomarker for chemotherapy outcome prediction.

## Acknowledgments

We thank everyone who contributed to this work: Dr. Hans E. Fjøsne and Dr. Torill E. Sjøbakk for recruiting patients; Dr. Agnes Østlie and Dr. Rebecca Rakow-Penner for supervising tumor delineation; Ingrid Framås Syversen; Dr. Jose R. Teruel for contributions to the image processing, and Dr. Anders M. Dale for kindly giving us access to the preprocessing software used for the Protocol II data. The histological sample preparation and whole-slide image scanning service was provided by the Cellular and Molecular Imaging Core Facility (CMIC), Norwegian University of Science and Technology (NTNU).

## Conflict of Interest

Author I.V. works for Multimodal Imaging Services Corporation, dba HealthLytx (San Diego, CA), but there are no conflicts of interest in relation to the current study.

## References

1. Bray F, Ferlay J, Soerjomataram I, Siegel RL, Torre LA, Jemal A. Global cancer statistics 2018: GLOBOCAN estimates of incidence and mortality worldwide for 36 cancers in 185 countries. *CA Cancer J Clin* 2018; 68:394–424.
2. Elston CW, Ellis IO. Pathological prognostic factors in breast cancer. I. The value of histological grade in breast cancer: Experience from a large study with long-term follow-up. *Histopathology* 1991;19: 403–410.
3. Norsk Bryst Cancer Grupper (NBCG) arbeidsutvalg; Naume B, Aas T, Lundgren S, Schlichting E, Eikesdal HP. Nasjonalt handlingsprogram med retningslinjer for diagnostikk, behandling og oppfølging av pasienter med brystkreft. HelseDirektoratet 2017.
4. Goldhirsch A, Wood WC, Coates AS, et al. Strategies for subtypes—Dealing with the diversity of breast cancer: Highlights of the St Gallen International Expert Consensus on the Primary Therapy of Early Breast Cancer 2011. *Ann Oncol* 2011;22:1736–1747.
5. Theocharis AD, Skandalis SS, Gialeli C, Karamanos NK. Extracellular matrix structure. *Adv Drug Del Rev* 2016;97:4–27.
6. Conklin MW, Keely PJ. Why the stroma matters in breast cancer: Insights into breast cancer patient outcomes through the examination of stromal biomarkers. *Cell Adh Migr* 2012;6:249–260.
7. Hanahan D, Weinberg Robert A. Hallmarks of cancer: The next generation. *Cell* 2011;144:646–674.
8. Provenzano PP, Inman DR, Eliceiri KW, et al. Collagen density promotes mammary tumor initiation and progression. *BMC Med* 2008; 6:11.
9. Provenzano PP, Eliceiri KW, Campbell JM, Inman DR, White JG, Keely PJ. Collagen reorganization at the tumor-stromal interface facilitates local invasion. *BMC Med* 2006;4:38.
10. Boyd NF, Martin LJ, Bronskill M, Yaffe MJ, Duric N, Minkin S. Breast tissue composition and susceptibility to breast cancer. *J Natl Cancer Inst* 2010;102:1224–1237.
11. Brabrand A, Kariuki II, Engstrøm MJ, et al. Alterations in collagen fibre patterns in breast cancer. A premise for tumour invasiveness? *APMIS* 2015;123:1–8.
12. Guo Y, Cai Y-Q, Cai Z-L, et al. Differentiation of clinically benign and malignant breast lesions using diffusion-weighted imaging. *J Magn Reson Imaging* 2002;16:172–178.
13. Vidić I, Egnell L, Jerome NP, et al. Support vector machine for breast cancer classification using diffusion-weighted MRI histogram features: Preliminary study. *J Magn Reson Imaging* 2018;47:1205–1216.
14. Onishi N, Kanao S, Kataoka M, et al. Apparent diffusion coefficient as a potential surrogate marker for Ki-67 index in mucinous breast carcinoma. *J Magn Reson Imaging* 2015;41:610–615.
15. Sun K, Chen X, Chai W, et al. Breast cancer: Diffusion kurtosis MR imaging—Diagnostic accuracy and correlation with clinical-pathologic factors. *Radiology* 2015;277:46–55.
16. Tamura T, Usui S, Murakami S, et al. Comparisons of multi  $b$ -value DWI signal analysis with pathological specimen of breast cancer. *Magn Reson Med* 2012;68:890–897.
17. Kakkad S, Zhang J, Akhbardeh A, et al. Collagen fibers mediate MRI-detected water diffusion and anisotropy in breast cancers. *Neoplasia* 2016;18:585–593.
18. Teruel JR, Goa PE, Sjøbakk TE, Østlie A, Fjøsne HE, Bathen TF. Diffusion weighted imaging for the differentiation of breast tumors: From

- apparent diffusion coefficient to high order diffusion tensor imaging. *J Magn Reson Imaging* 2016;43:1111–1121.
19. Teruel JR, Fjøsne HE, Østlie A, et al. Inhomogeneous static magnetic field-induced distortion correction applied to diffusion weighted MRI of the breast at 3T. *Magn Reson Med* 2015;74:1138–1144.
  20. Vidić I, Jerome NP, Bathen TF, Goa PE, While PT. Accuracy of breast cancer lesion classification using intravoxel incoherent motion diffusion-weighted imaging is improved by the inclusion of global or local prior knowledge with Bayesian methods. *J Magn Reson Imaging* 2019;50:1478–1488.
  21. Teruel JR, Goa PE, Sjøbakk TE, Østlie A, Fjøsne HE, Bathen TF. A simplified approach to measure the effect of the microvasculature in diffusion-weighted MR imaging applied to breast tumors: Preliminary results. *Radiology* 2016;281:373–381.
  22. Zitová B, Flusser J. Image registration methods: A survey. *Image Vis Comput* 2003;21:977–1000.
  23. Holland D, Kuperman JM, Dale AM. Efficient correction of inhomogeneous static magnetic field-induced distortion in echo planar imaging. *Neuroimage* 2010;50:175–183.
  24. McDonald CR, White NS, Farid N, et al. Recovery of white matter tracts in regions of peritumoral FLAIR hyperintensity with use of restriction spectrum imaging. *Am J Neuroradiol* 2013;34:1157–1163.
  25. Karunamuni RA, Kuperman J, Seibert TM, et al. Relationship between kurtosis and bi-exponential characterization of high b-value diffusion-weighted imaging: Application to prostate cancer. *Acta Radiol* 2018; 59:1523–1529.
  26. Xia Y, Farquhar T, Burton-Wurster N, Ray E, Jelinski LW. Diffusion and relaxation mapping of cartilage-bone plugs and excised disks using microscopic magnetic resonance imaging. *Magn Reson Med* 1994;31: 273–282.
  27. Edden RAE, Smith SA, Barker PB. Longitudinal and multi-echo transverse relaxation times of normal breast tissue at 3 Tesla. *J Magn Reson Imaging* 2010;32:982–987.
  28. Rakow-Penner R, Daniel B, Yu H, Sawyer-Glover A, Glover GH. Relaxation times of breast tissue at 1.5T and 3T measured using IDEAL. *J Magn Reson Imaging* 2006;23:87–91.
  29. Jayakumar PN, Srikanth SG, Chandrashekar HS, Subbakrishna DK. T2 relaxometry of ring lesions of the brain. *Clin Radiol* 2007;62:370–375.
  30. Bankhead P, Loughrey MB, Fernández JA, et al. QuPath: Open source software for digital pathology image analysis. *Sci Rep* 2017;7:16878.
  31. Surov A, Meyer HJ, Wienke A. Correlation between apparent diffusion coefficient (ADC) and cellularity is different in several tumors: A meta-analysis. *Oncotarget* 2017;8:59492–59499.
  32. Tamura T, Usui S, Murakami S, et al. Biexponential signal attenuation analysis of diffusion-weighted imaging of breast. *Magn Reson Med Sci* 2010;9:195–207.
  33. Fullerton GD, Cameron IL, Ord VA. Orientation of tendons in the magnetic field and its effect on T2 relaxation times. *Radiology* 1985;155: 433–435.
  34. Fullerton GD, Nes E, Amurao M, Rahal A, Krasnoselskaia L, Cameron I. An NMR method to characterize multiple water compartments on mammalian collagen. *Cell Biol Int* 2006;30:66–73.
  35. Fullerton GD, Rahal A. Collagen structure: The molecular source of the tendon magic angle effect. *J Magn Reson Imaging* 2007;25:345–361.
  36. Jerome NP, Boulton JKR, Orton MR, et al. Characterisation of fibrosis in chemically-induced rat mammary carcinomas using multi-modal endogenous contrast MRI on a 1.5T clinical platform. *Eur Radiol* 2018;28: 1642–1653.
  37. Xu S, Xu H, Wang W, et al. The role of collagen in cancer: From bench to bedside. *J Transl Med* 2019;17:309.
  38. Whatcott CJ, Diep CH, Jiang P, et al. Desmoplasia in primary tumors and metastatic lesions of pancreatic cancer. *Clin Cancer Res* 2015;21: 3561–3568.
  39. Cheang MCU, Chia SK, Voduc D, et al. Ki67 Index, HER2 status, and prognosis of patients with luminal B breast cancer. *J Natl Cancer Inst* 2009;101:736–750.
  40. Goldhirsch A, Ingle JN, Gelber RD, et al. Thresholds for therapies: Highlights of the St Gallen International Expert Consensus on the Primary Therapy of Early Breast Cancer 2009. *Ann Oncol* 2009;20: 1319–1329.